ELSEVIER

Journal of Fluids and Structures 19 (2004) 17–27

JOURNAL OF FLUIDS AND STRUCTURES

www.elsevier.nl/locate/jnlabr/yjfls

Transonic limit cycle oscillation analysis using reduced order aerodynamic models

E.H. Dowell*, J.P. Thomas, K.C. Hall

Department of Mechanical Engineering and Materials Science, Duke University, Box 90300, Durham, NC 27708-0300, USA

Received 14 May 2001; accepted 23 July 2003

Abstract

Limit cycle oscillations have been observed in flight operations of modern aircraft, wind tunnel experiments and mathematical models. Both fluid and structural nonlinearities are thought to contribute to these phenomena. With recent advances in reduced order aerodynamic modeling, it is now feasible to analyze limit cycle oscillations that may occur in transonic flow including the effects of structural and fluid nonlinearities. In this paper an airfoil with control surface freeplay (a common structural nonlinearity) is used to investigate transonic flutter and limit cycle oscillations. The reduced order aerodynamic model used in this paper assumes the shock motion is small and in proportion to the structural motions.

Keywords: Unsteady aerodynamics; Aeroelasticity; Reduced order models; Limit cycle oscillations

1. Introduction

The principal focus of this paper is on the transonic aeroelastic behavior of an airfoil with control surface freeplay including flutter and limit cycle oscillations. In this work, we assume the shock motion is sufficiently small such that it is (linearly) proportional to the airfoil motion, e.g. airfoil motions are less than the equivalent of one degree in angle-of-attack.

Using an Euler/computational fluid dynamic (CFD)-based reduced order aerodynamic model, a thorough study of the flutter boundary with Mach number is first presented in the absence of freeplay. Particularly noteworthy are the rapid changes of flutter modal content in the transonic range. This is attributed in part to the rapid changes of center of pressure location as the mean shock position changes with Mach number. These changes in the modal response content are also found in the limit cycle oscillations (LCO) which are encountered when control surface freeplay is present. Indeed for LCO, the modal content may change at a fixed Mach number when the dynamic pressure or flow density is varied.

Below $M_\infty = 0.80$, the LCO and flutter oscillations are qualitatively similar to those found at low Mach number where earlier computational studies and experiments have been carried out. However, the response behavior in the transonic flow regime is notably different. Of special interest is the occurrence of flutter in a narrow range of Mach number for pitch and flap (control surface) dominated motions. Moreover, beyond a certain high transonic Mach number (after the mean shock position reaches the trailing edge of the airfoil), neither flutter nor limit cycle oscillation occurs.

*Corresponding author.
E-mail addresses: dowell@mail.ee.duke.edu (E.H. Dowell), jthomas@duke.edu (J.P. Thomas), hall@duke.edu (K.C. Hall).

0889-9746/$ - see front matter © 2003 Elsevier Ltd. All rights reserved.
doi:10.1016/j.jfluidstructs.2003.07.018

Nomenclature

a, a_f	location of airfoil elastic axis and flap hinge axis, see Fig. 1
b, c	semi-chord and chord, respectively
c_l, c_m, c_n	coefficients of lift, airfoil moment
h, α, β	airfoil plunge, airfoil pitch, and flap pitch degrees of freedom, respectively
I_α, I_β	second moment of inertia of airfoil about elastic axis and of flap about flap hinge axis, respectively
j	$\sqrt{-1}$
K_h, K_α, K_β	airfoil plunge stiffness, airfoil torsional stiffness about elastic axis, and flap torsional stiffness about hinge axis, respectively
M_∞	freestream Mach number
M	airfoil sectional mass including effect of mass of experimental model supports
m	airfoil sectional mass
r_α, r_β	radius of gyration of airfoil about elastic axis and of flap about flap hinge axis, respectively, $r_\alpha^2 = I_\alpha/mb^2, r_\beta^2 = I_\beta/mb^2$
S_α, S_β	first moment of inertia of airfoil about elastic axis and of flap about flap hinge axis, respectively
U_∞	freestream velocity
V	reduced velocity $V = U_\infty/\sqrt{\mu}\omega_\alpha b$
x_α, x_β	airfoil and flap static unbalance, $x_\alpha = S_\alpha/mb$, $x_\beta = S_\beta/mb$
α_0	airfoil steady (mean) background flow angle-of-attack
δ	freeplay region of flap
μ	mass ratio, $m/\pi\rho_\infty b^2$
ρ_∞	freestream density
τ_β	elastic torque in flap
$\omega, \bar{\omega}$	frequency and reduced frequency based on airfoil chord, $\bar{\omega} = \omega c/U_\infty$
$\omega_h, \omega_\alpha, \omega_\beta$	uncoupled natural frequency of plunging, pitching about elastic axis, and of flap rotation about flap hinge axis, respectively

2. Significance of LCO

LCO is known to occur on various operational aerospace flight vehicles. This has been a source of serious concern since there are no analysis techniques available that have predicted LCO in an operational aircraft. There have been some semi-empirical techniques developed to correlate with LCO that have been observed in flight, and these are useful for understanding the LCO that has occurred (Cunningham, 1999). However these techniques are not as satisfactory for the design of a new vehicle or the substantial modification of an existing one, e.g. new stores to be carried by an aircraft.

In wind tunnel tests of flight vehicle prototypes, LCO has been notably absent for the most part. This is perhaps not altogether surprising since wind tunnel scale models have been designed based upon linear aeroelastic concepts. Such wind tunnel models and tests have been used successfully for many years to investigate flutter (the onset of a dynamic linear instability). However, they are inherently unable to predict a nonlinear phenomenon such as LCO unless designed with LCO in mind.

In this regard, it should be noted that LCO may be beneficial as well as detrimental. Without the nonlinearities that lead to LCO, the onset of flutter may lead to catastrophic failure of the structure. Hence if we can understand and predict LCO, perhaps, we can take advantage of these nonlinearities to shape more favorable responses of the aircraft leading to enhanced safety and performance.

3. Technical discussion

3.1. Sources of nonlinearities

The principal sources of the nonlinearities essential to the LCO are a subject of current debate among the experts in the field. The candidate sources are several; for the fluid: (i) shock motions; (ii) separated flow motions; for the structure: (i) freeplay; (ii) geometric, e.g., a nonlinear relationship between strain and displacement; (iii) material, e.g., dry friction damping.

Also there is a further distinction between a static versus a dynamic nonlinearity. An important example of this is the role of a shock wave in the fluid. If a shock is present, then its creation is the result of a dynamic nonlinear process. However, once a steady flow is established, and if the airfoil motion is sufficiently small, then the shock motion will also be small and proportional to the airfoil motion. Hence in this situation, the shock itself represents a nonlinear static (time independent) equilibrium and the motion may be treated as a dynamically linear perturbation about the mean shock position. In the following discussion, we assume a dynamically linear model of the shock motion, but also include a structural (dynamic) nonlinearity, i.e., freeplay in the connection of the control surface to the airfoil.

3.2. Airfoil with control surface freeplay model

A sketch of the configuration is shown in Fig. 1. It is a conventional typical section model except that the spring that attaches the control surface to the airfoil has a nonlinear freeplay. The elastic restoring torque or moment provided by this spring is shown in Fig. 2 as a function of control surface or flap rotation angle, β. The freeplay angle is δ. Note that when β is less than δ, there is zero restoring torque, while for β much greater than δ, the spring stiffness is the nominal value in the absence of freeplay. The freeplay may be thought of as creating a stiffness or (uncoupled) natural frequency of the spring that varies as a function of flap amplitude. This interpretation is shown in Fig. 3. Here the flap uncoupled natural frequency normalized by the nominal value in the absence of freeplay is shown as a function of flap amplitude, β, normalized by the freeplay angle, δ. Note that given a certain flap amplitude, there is a corresponding "equivalent" flap frequency. Of course, for a linear system the control surface or flap frequency would have a fixed value independent of flap amplitude.

Thus conceptually and computationally one may proceed as follows. First, one determines the neutrally stable motions of the system in the absence of freeplay for various flap frequencies from zero to the nominal value. Then one determines the corresponding neutrally stable nonlinear limit cycle motion, namely the flap amplitude, from Fig. 3. More details of this procedure will be given later including the construction of the linear instability or flutter boundary for this system, which serves as a basis for determining the limit cycle oscillations.

This approach has been used successfully at low Mach numbers, and the theoretical results correlated with experiments (Conner et al., 1997; Tang et al., 1998), and also with theoretical results from time simulations. To extend these earlier calculations to transonic flow requires a substantially more sophisticated, but still computationally efficient aerodynamic model. Fortunately one is available as is described later.

3.3. The structural model

This model has three degrees of freedom in plunge, pitch of the airfoil, and flap of the control surface. The equations are well known (Conner et al., 1997; Tang et al., 1998) with the only novelty being the freeplay stiffness associated with the rotational spring connected from the flap or control surface to the main airfoil

$$\begin{aligned} &M\ddot{h} + S_\alpha \ddot{\alpha} + S_\beta \ddot{\beta} + K_h h = -L, \\ &S_\alpha \ddot{h} + I_\alpha \ddot{\alpha} + [I_\beta + b(a_f - a)S_\beta]\ddot{\beta} + K_\alpha \alpha = M_\alpha, \\ &S_\beta \ddot{h} + [I_\beta + b(a_f - a)S_\beta]\ddot{\alpha} + I_\beta \ddot{\beta} + K_\beta \beta = M_\beta. \end{aligned} \tag{1}$$

Considering harmonic motion with characteristic frequency ω, this system of equations may be written in the frequency domain as

$$\left(-\bar{\omega}^2[M] + \frac{4}{\mu V^2}[K]\right)\{u\} = \frac{4}{\pi\mu}\{f\}, \tag{2}$$

where

$$[M] = \begin{bmatrix} M/m & x_\alpha & x_\beta \\ x_\alpha & r_\alpha^2 & (a_f - a)x_\beta + r_\beta^2 \\ x_\beta & (a_f - a)x_\beta + r_\beta^2 & r_\beta^2 \end{bmatrix}, \tag{3}$$

$$[K] = \begin{bmatrix} (\omega_h/\omega_\alpha)^2 & 0 & 0 \\ 0 & r_\alpha^2 & 0 \\ 0 & 0 & r_\beta^2(\omega_\beta/\omega_\alpha)^2 \end{bmatrix}, \tag{4}$$

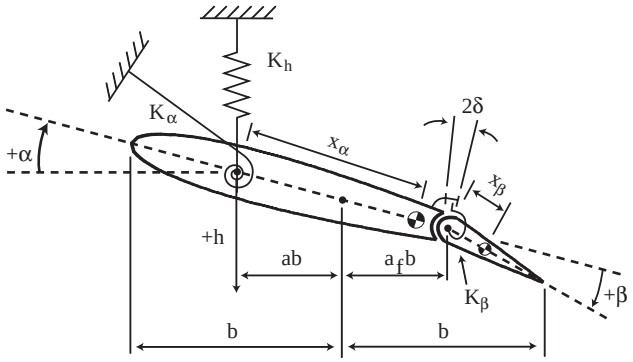

Fig. 1. Airfoil with control surface configuration.

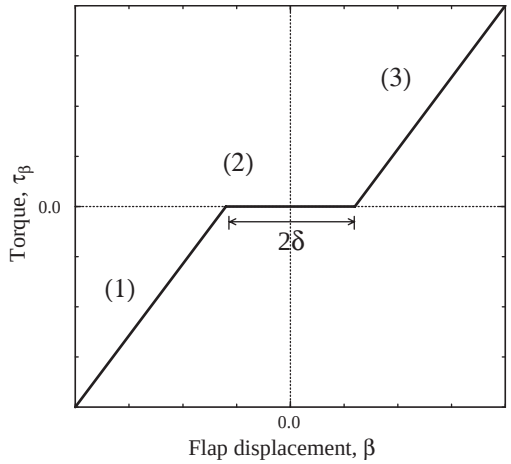

Fig. 2. Restoring moment as a function of control surface or flap rotation angle.

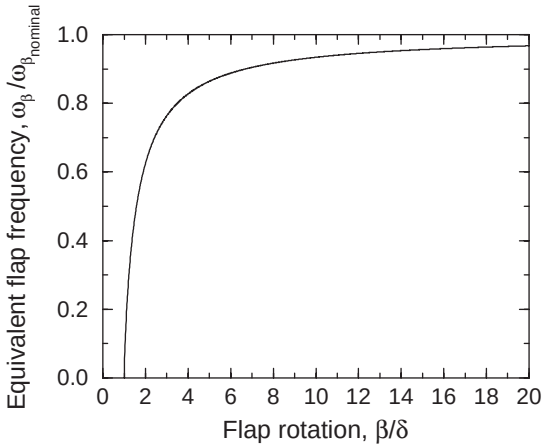

Fig. 3. Equivalent nonlinear flap frequency versus flap rotation.

$$\{u\} = \begin{Bmatrix} \bar{h}/b \\ \bar{\alpha} \\ \bar{\beta} \end{Bmatrix}, \quad \{f\} = \begin{Bmatrix} -\bar{c}_l \\ 2\bar{c}_m \\ 2\bar{c}_n \end{Bmatrix} \tag{5}$$

and $\bar{h} = h e^{i\omega t}, \bar{c}_l = c_l e^{i\omega t}$, etc. We have omitted structural damping in these equations, but that is readily included if desired.

The nonlinear relationship between elastic torque in the flap spring and the flap displacement is given by

$$\tau_\beta = \begin{cases} 0 & |\beta| \leqslant \delta, \\ K_\beta(\beta - \delta) & |\beta| > \delta, \end{cases} \tag{6}$$

where K_β is the nominal linear flap spring stiffness, and δ is the half-angle that defines the range of the freeplay; see Fig. 2.

With Eq. (6), a describing function or harmonic balance relationship may be derived (Tang et al., 1998) that provides a relationship between the effective uncoupled flap frequency and the amplitude of the assumed harmonic motion; see Fig. 3. We emphasize that the harmonic balance or describing function methodology can be used to treat not only freeplay, but other structural nonlinearities and also fluid nonlinearities as well.

3.4. Computational fluid dynamic (CFD) modeling and its modal decomposition

A typical CFD model is very large in terms of the number of equations required to be solved. And this makes such models problematical for aeroelastic (and some other) analyses. For example, the CFD model used in the present work is based upon the Euler equations of fluid mechanics and has a spatial grid of 65×97 (6035) mesh points. At each grid point there are four fluid variables to be determined. Thus the CFD model per se has about 25 000 unknowns to be determined by solving 25 000 equations. This is a doable task if the structural motion is known. However, if this CFD model is to be combined with a set of structural equations of motion, and solutions are to be found the computational feasibility issue. These, as well as the method to be described and used here, are discussed in more depth in Hall et al. (2000) and Thomas et al. (1999). Among these methods are variations on the notion of a Padé approximate.

The method used here is based upon the observation that virtually all CFD models can be thought of as having a modal composition. The simplest conceptual set of modes is perhaps the fluid or aerodynamic eigenmodes of the CFD model, and these modes have been used successfully in creating reduced order models (ROM) that are computationally and conceptually attractive (Hall et al., 2000; Dowell and Hall, 2001; Thomas et al., 1999, 2003).

However, it turns out that determining the aerodynamic eigenmodes of a large CFD model is itself a challenging task. Hence a method called the proper orthogonal decomposition (POD) (Hall et al., 2000; Thomas et al., 1999, 2003; Kim, 1998) has been developed. The first use of this method in an Euler based aerodynamic context was demonstrated by Romanowski and Dowell (1994). In this method, by using a time history or frequency response of the CFD model to a known structural input, one may construct a small set of modes or basis functions, typically less than 100. Using these modes, one can reconstitute and very substantially reduce the size of the CFD model with essentially no loss in accuracy or physical content. This is the approach used here.

For the present analysis, 63 POD modes are found from the frequency responses (aerodynamic transfer functions) in flap, pitch and plunge, respectively, at 21 frequencies at each Mach number studied using the original CFD model. Based upon previous experience, one might use an even smaller number of aerodynamic modes than this. However, even with this generous number of modes, the computations described below were all done in a few days.

The computational grid used for the CFD model is shown in Figs. 4 and 5 shows the chordwise steady flow pressure distributions for several Mach numbers. Note the presence of the shock at $M_\infty = 0.80$, 0.85, and 0.90.

3.5. Linear instability (flutter)

First, consider the flutter behavior for this system in the absence of freeplay. The stability of this system was assessed by constructing a root locus (migration of the true aeroelastic eigenvalues) as a function of the nondimensional airspeed or dynamic pressure for each Mach number. The usual structural and flow parameters are defined in Table 1. These are typical and correspond to the theoretical and experimental models (Cunningham, 1999; Conner et al., 1997).

A representative root locus result is shown in Fig. 6 for $M_\infty = 0.80$. Root locus results are available for all Mach numbers used to construct the flutter boundary, which is shown in Fig. 7. Consider first Fig. 6. The eigenvalues in this root locus are those of the coupled fluid/structural (aeroelastic) system. However, the roots that originate as structural modes at low values of velocity or dynamic pressure are readily identified and labeled in Fig. 6. The vertical axis is the

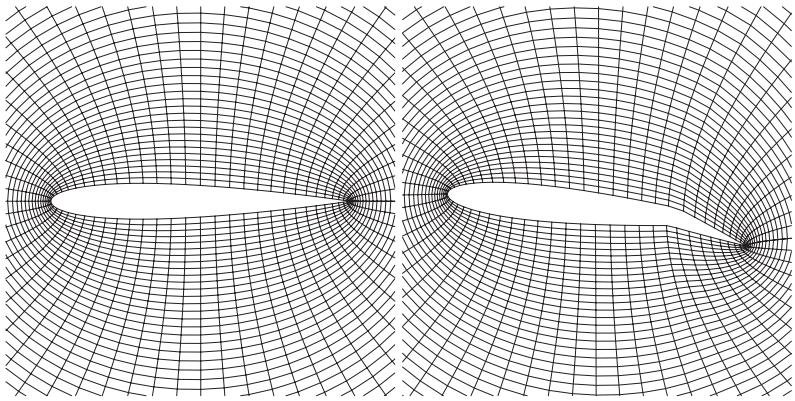

Fig. 4. NACA 0012 grid: 64×97 computational nodes, outer boundary radius = 15 cm.

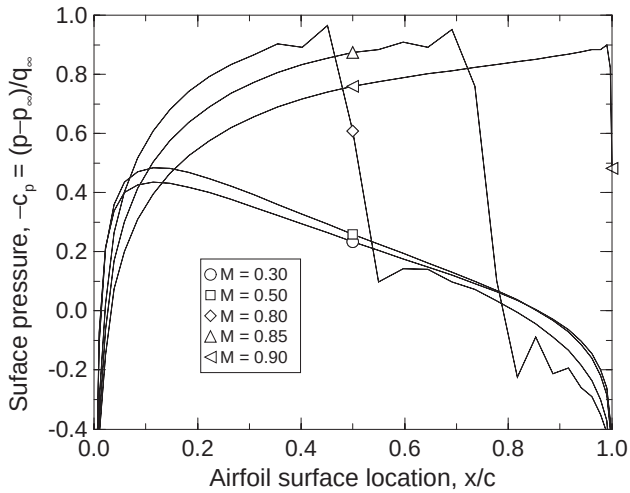

Fig. 5. Computed NACA 0012 steady flow surface pressure distributions: $\alpha_0 = 0.0$ (deg).

imaginary part of the eigenvalue or frequency, and the horizontal axis displays the real part or rate of growth (if positive) or decay (if negative) of the oscillations associated with each root or eigenvalue.

Note especially that the "plunge" aeroelastic mode has a root that for low "gain" (or flow velocity or dynamic pressure) moves to the left and becomes more stable. But then as the flow velocity increases, it reverses direction and moves into the right half plane becoming unstable. And then at even higher velocities, it moves back into the left-hand plane and becomes stable again. However by then, the pitch mode has moved into the right half plane and become unstable. Hence the aeroelastic system remains unstable once the plunge mode becomes again stable at this velocity and Mach number.

All the other roots in this figure, which appear to originate from near the origin and move radially to the left with increasing flow velocity, are essentially aerodynamic roots. These roots all move off into the left half plane indicating they are always stable and increasingly so as the dynamic pressure increases. On occasion an aerodynamic root may become unstable, however, though not for the parameters studied in this work.

As the Mach number becomes higher, the most critical root may change. For example, at $M_\infty = 0.85$ the pitch root becomes unstable first, and for $M_\infty = 0.90$, it is the flap root. At yet higher Mach numbers, no roots become unstable. For brevity these other root loci are omitted here.

Taking all of this information from the root loci at various Mach numbers, the flutter boundary trend with Mach number can be determined, and is presented in Fig. 7(a). There are several interesting features to this flutter boundary. Up to $M_\infty = 0.80$, the root-loci are rather similar, and it is always the plunge root that is critical for flutter. Starting at

Table 1
Structural parameters NACA 0012 airfoil with control surface

Structural parameters	
b= 0.127 m	$\mu = 25.24$
$m^a = 1.567$ kg/m	$x_\alpha = 0.4316$
$\rho_\infty = 1.225$ kg/m^3	$r_\alpha^2 = 0.5331$
$a = -0.5$	$x_\beta = 0.01985$
$a_f = 0.5$	$r_\beta^2 = 0.01292$
Uncoupled frequencies (Hz)	Coupled frequencies (Hz)
$\omega_h = 4.59$	$\omega_h = 4.45$
$\omega_\alpha = 6.04$	$\omega_\alpha = 9.21$
$\omega_\beta = 12.54$	$\omega_\beta = 19.44$

[a] Plunge inertia corrected for experimental support mass.

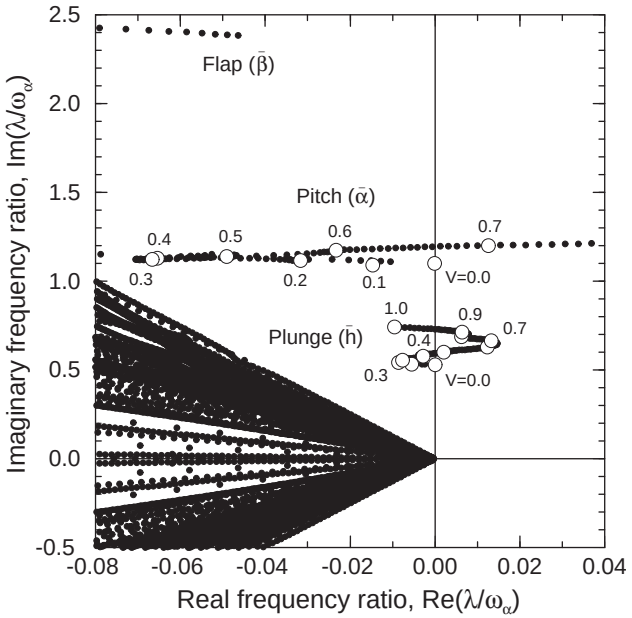

Fig. 6. Aeroelastic system eigenvalue root-loci: $M_\infty = 0.80$, $\alpha_0 = 0.0$ (deg).

$M_\infty = 0.80$, the pitch root also shows instability, and at $M_\infty = 0.825$ and 0.85, it is most critical for flutter. At $M_\infty = 0.875$ and 0.90, the flap mode is most critical for flutter, and for M_∞=0.925 to at least $M_\infty = 1.1$, no flutter is observed for a nondimensional flow velocity up to at least one. The corresponding frequencies of the flutter oscillations are shown in Fig. 7(b). Note that in Fig. 7 when two data points are shown for say the plunge root at a fixed Mach number, the lower velocity point is when flutter begins, and the higher velocity point is when the root returns to the stable left half plane and flutter ceases in that root.

Note also the narrow range of Mach number where the change in flutter mode occurs. Results of this type have been observed in experiments where they are called "chimneys" (Silva, 2000).

3.6. Limit cycle oscillations

Now the freeplay is added to the model and thus LCO may occur. As is perhaps obvious from physical intuition, when freeplay is added, the stiffness of the control surface freeplay is reduced for small motions. Hence one expects limit cycle oscillations to occur below the flutter boundary, i.e. at flow velocities less than those shown in Fig. 7(a). Indeed, a

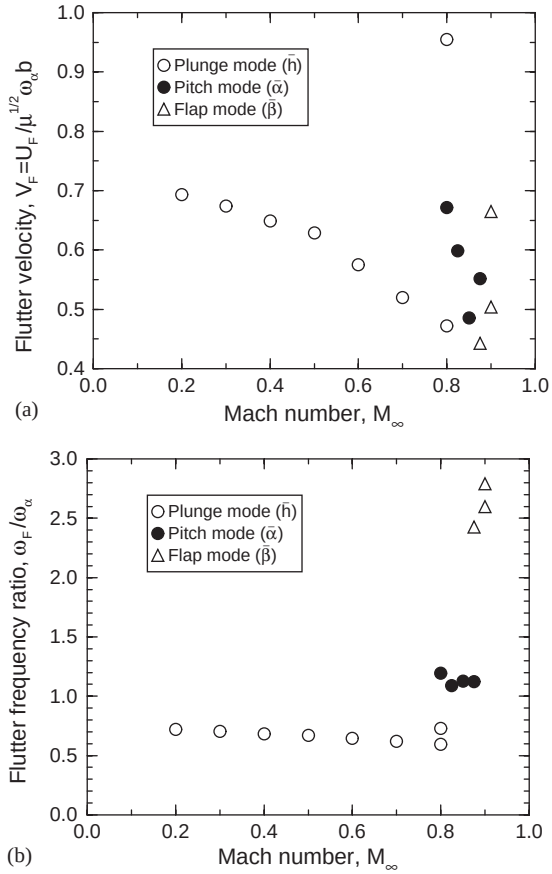

Fig. 7. Mach number flutter trend: $\alpha = 0.0$ (deg): (a) Flutter speed; (b) flutter frequency.

few moments of reflection may lead one to expect that once the linear flutter boundary shown in Fig. 7(a) is exceeded, then exponentially explosive flutter will occur when the nonlinearity is due to freeplay. That is found to be the case as shown by the present analysis and also by the analysis and experiments of Conner et al. (1997) and Tang et al. (1998).

To compute the LCO one proceeds as follows. For all other parameters fixed including Mach number, the flutter velocity is determined from a linear flutter analysis as a function of (uncoupled) flap natural frequency (or equivalently spring stiffness). Since the flap frequency (or stiffness) is known as a function of flap amplitude, see Fig. 3 (or 2), we immediately can determine from these two results (by cross-plotting), the flap amplitude for neutrally stable nonlinear motions (LCO) as a function of flow velocity. As an example for $M_\infty = 0.80$, see Fig. 8. In Fig. 8(a), the "flutter" or flow velocity at which neutrally stable oscillations may occur is shown as a function of flap frequency. Using Fig. 3, which shows the nonlinear dependence of flap frequency as a function of flap amplitude, Fig. 8(b) may be constructed. This shows LCO amplitude as a function of flow velocity. The corresponding "flutter" frequency and the LCO frequency are shown in Figs. 8(c) and 8(d), respectively.

A comment on this method is appropriate here. The reader familiar with the harmonic balance approach will recognize that a single harmonic approximation has been used to describe the freeplay nonlinearity. This approach is more fully described in the present context in Tang et al. (1998). Of course, this is a classical procedure for nonlinear systems; though it is not often used for systems with as many degrees of freedom as the present one. The results of Tang et al. (1998) confirm that the harmonic balance approach gives results in good agreement with those obtained from time marching solutions that include all harmonics, as well as the results from experiments.

The results of Fig. 8 have several interesting features. First of all, the limit cycle amplitude is normalized by the freeplay angle, δ. The theory predicts and experiments agree, see Tang et al. (1998), that when the results are normalized in this manner, they are universal. That is, the limit cycle amplitude is proportional to the freeplay angle. Secondly, the lowest velocity at which LCO may occur corresponds to the minimum flutter velocity that occurs at a certain flap

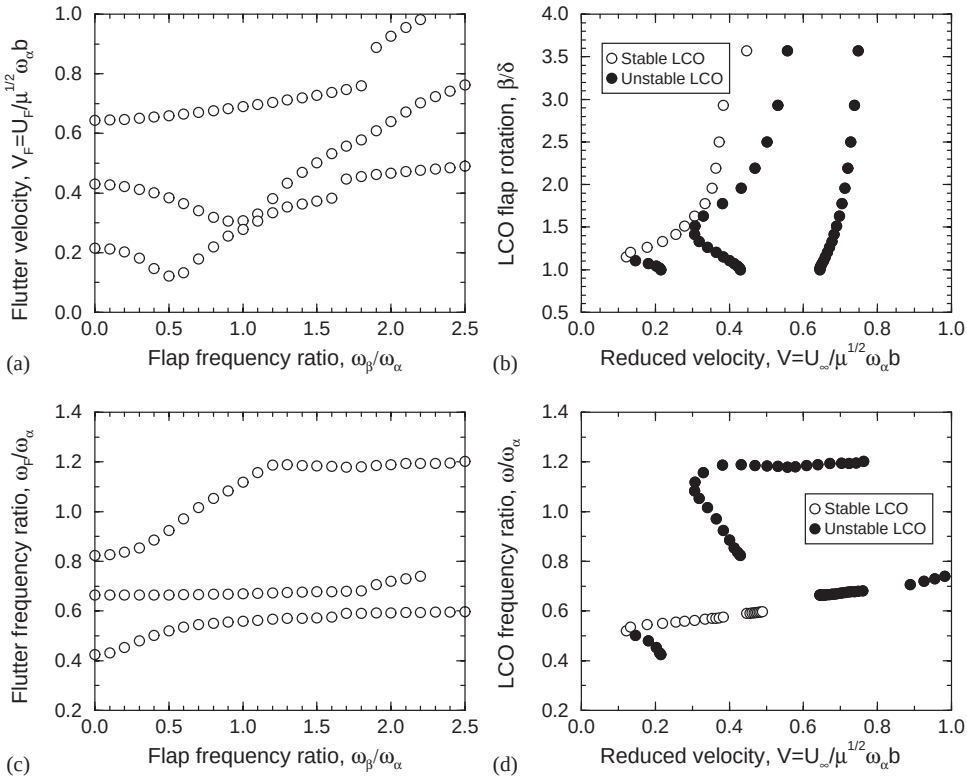

Fig. 8. Limit cycle behaviour: $M_\infty = 0.80$, $\alpha = 0.0$ (deg): (a) Flutter velocity; (b) LCO flap rotation; (c) flutter frequency ratio; (d) LCO frequency ratio.

frequency. See Fig. 8(a) and then compare the lowest velocity for LCO in Fig. 8(b). Strictly speaking, a finite disturbance is required to generate LCO at this lowest velocity and for a small velocity range thereafter. LCOs for any disturbance, no matter how small, will only occur when the flutter velocity for a flap frequency of zero is exceeded. Again compare Figs. 8(a) and (b). The unstable LCOs, which are shown along with the stable LCOs (those that are observed in an experiment), provide a measure of the level of disturbance required to initiate the LCO at the lower flow velocities. In practice such disturbances are usually present in wind tunnel experiments and flight operations.

The results of Fig. 8 are typical until one reaches the higher transonic Mach numbers where linear theory predicts flutter will cease. At the highest Mach number considered here where flutter and LCO may occur, $M_\infty = 0.90$, the LCO has a somewhat different character; see Fig. 9. Again the LCO is first encountered at the minimum velocity at which flutter will occur over the range of flap frequencies. But now the corresponding flap frequency is zero; see Fig. 9(a). Moreover, when the flow velocity increases to higher values, there are two stable limit cycles as well as one unstable limit cycle. The nature of the disturbances to the system would determine which of these two LCO would be observed in a wind tunnel experiment or in stable flight. Note that the LCO branch with the larger amplitude will again move to amplitudes with very large values (to infinity according to the present theoretical model) when the flow velocity approaches the linear flutter velocity.

4. Conclusions

The transonic flutter and limit cycle oscillations of an airfoil with control surface freeplay have been determined using a new aerodynamic modelling technique that provides greater physical insight and understanding by tracing the true root locus of the corresponding linear aeroelastic system. This in turn enables a very computationally efficient harmonic balance technique to be used in determining the nonlinear limit cycle oscillations.

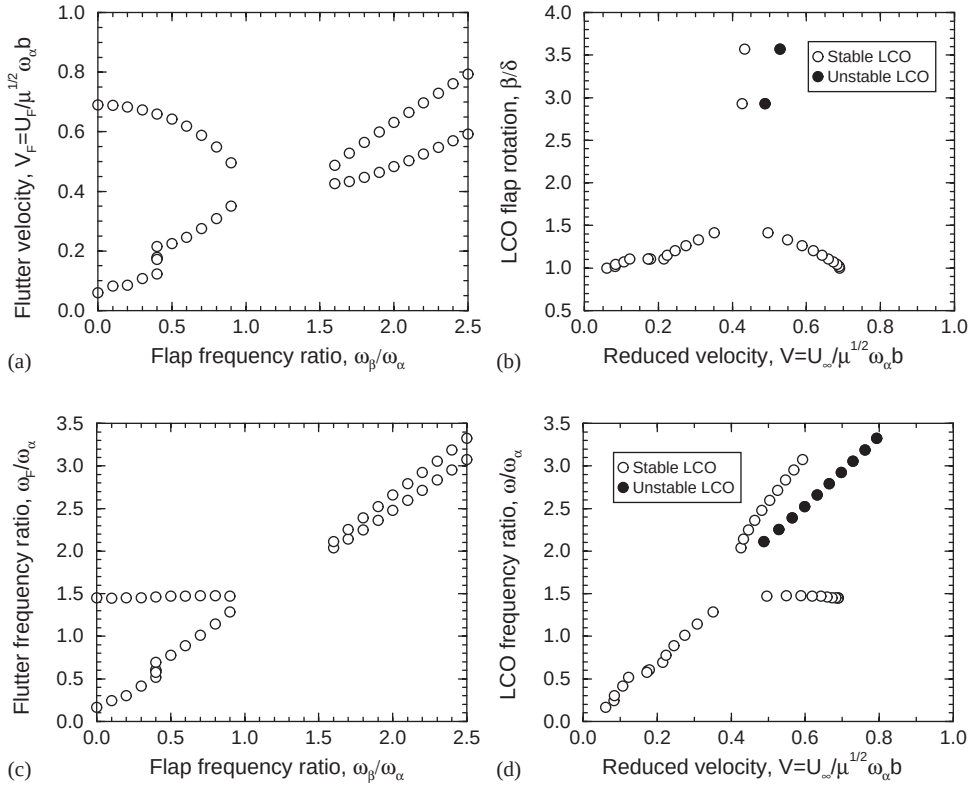

Fig. 9. Limit cycle behaviour: $M_\infty = 0.90$, $\alpha = 0.0$ (deg): (a) Flutter velocity; (b) LCO flap rotation; (c) flutter frequency ratio; (d) LCO frequency ratio.

New physical insights gained include the rapid change in flutter mode that occurs in the transonic Mach number range. This phenomenon has been observed in experiments (Silva, 2000), but has not been previously predicted theoretically. With respect to LCO, these are the first results available in the transonic range for the configuration studied. The model also predicts significant changes in LCO behavior as a function of Mach number. However, these are as yet unconfirmed by experiments. Up to high subsonic Mach numbers, the flutter and LCO results are similar to those previously found at low Mach numbers.

5. Future work

There are no available time marching solutions for the configuration studied in the present paper. However, the authors have compared time marching solutions and harmonic balance solutions in the incompressible flow range for the present nonlinear structural model with control surface freeplay and results from the two methods closely correspond; see Tang et al. (1998). We have also compared results for flutter and LCO from harmonic balance solutions to time marching solutions for other airfoil configurations where aerodynamic nonlinearities are dominant and again obtained good correlation between results from the two different approaches; see Hall et al. (2000) and Thomas et al. (2003).

Hence, we expect good correlation would be obtained in the present case between the results from our present harmonic balance analysis and those obtained from a time marching simulation. Yet it would be interesting to compare results from a time marching code to those obtained with the harmonic balance method for the present configuration. Of course an important motivation for the present work is that the frequency domain, harmonic balance method is computationally much more efficient than current time marching methods and that is why we have developed this method and prefer to use it.

Also, the first author and other colleagues have investigated the effect if a nonzero angle-of-attack, which can be important in applications. See for instance Kholodar and Dowell (1999). However, this effect has not yet been

investigated for the transonic case, though we would expect qualitatively similar results. For low Mach numbers we found what many practitioners have long observed and is perhaps intuitively expected, i.e., as the angle-of-attack is increased sufficiently the LCO oscillation disappears and the flutter boundary reverts to that associated with the nominal flap stiffness in the absence of freeplay. The nonlinear theory does provide an important quantitative measure of how much that angle-of-attack must be to suppress the LCO. For the low Mach number case it is about four times the freeplay angle, i.e., the larger the freeplay angle the larger the angle-of-attack must be to suppress LCO.

It would be very interesting to determine if magnitude of the angle-of-attack required to suppress LCO is larger or smaller for transonic flow than for low Mach numbers.

Acknowledgements

This work was supported by AFOSR Grant F49620-00-1-0030 and AFOSR Contract F49620-99-C-0050 (STTR). Dr Daniel Segalman and Dr Dean Mook are the responsible Program Managers. The authors would also like to thank Denis Kholodar for insightful discussions regarding material in this paper.

References

Conner, M.D., Tang, D.M., Dowell, E.H., Virgin, L.N., 1997. Nonlinear behavior of a typical airfoil section with control surface freeplay: a numerical and experimental study. Journal of Fluids and Structures 11, 89–109.

Cunningham, A.M., 1999. A generic nonlinear aeroelastic method with semi-empirical nonlinear unsteady aerodynamics. Technical Report AFRL-VA-WP-TR-1999-3014, Vol. 1 and 2, Air Force Research Laboratory.

Dowell, E.H., Hall, K.C., 2001. Modeling of fluid-structure interaction. Annual Reviews of Fluid Mechanics 33, 445–490.

Hall, K.C., Thomas, J.P., Dowell, E.H., 2000. Proper orthogonal decomposition technique for transonic unsteady aerodynamic flows. AIAA Journal 38 (10), 1853–1862.

Kholodar, D.B., Dowell, E.H., 1999. Behavior of airfoils with control surface freeplay at non-zero angles-of-attack. AIAA Journal 37 (5), 651–653.

Kim, T., 1998. Frequency-domain Karhunen-Loeve method and its application to linear dynamic systems. AIAA Journal 36 (11), 2117–2123.

Romanowski, M.C., Dowell, E.H., 1994. Using eigenmodes to form an efficient Euler based unsteady aerodynamics analysis. Presented at the ASME International Mechanical Engineering Congress and Exposition, Chicago, IL, November 1994.

Silva, W.A., 2000. Experimental steady and unsteady aerodynamic and flutter results for hsct semispan models. Presentation at the Aerospace Flutter and Dynamics Council Meeting at NASA Langley Research Center, May 2000.

Tang, D.M., Dowell, E.H., Virgin, L.N., 1998. Limit cycle behavior of an airfoil with a control surface. Journal of Fluids and Structures 12, 839–858.

Thomas, J. P., Dowell, E.H., Hall, K.C., 1999. Reduced-order aeroelastic modeling using proper-orthogonal decompositions. CEAS/AIAA/ICASE/NASA Langley International Forum on Aeroelasticity and Structural Dynamics, Williamsburg, Virginia, USA, June 1999.

Thomas, J.P., Dowell, E.H., Hall, K.C., 2003. Three-dimensional transonic aeroelasticity using proper orthogonal decomposition-based reduced-order models. Journal of Aircraft 40, 544–551.